CERN-TH-2024-215
FERMILAB-PUB-24-0938-T

Testing the Froggatt-Nielsen Mechanism with Lepton Violation – Supplemental Material

Claudia Cornella [1,*] David Curtin [2,†] Gordan Krnjaic [3,4,5,‡] and Micah Mellors [2,§]

[1] *Theoretical Physics Department, CERN, Geneva, Switzerland*
[2] *Department of Physics, University of Toronto, Canada*
[3] *Theoretical Physics Division, Fermi National Accelerator Laboratory, Batavia, IL, USA*
[4] *Department of Astronomy & Astrophysics, University of Chicago, Chicago, IL USA*
[5] *Kavli Institute for Cosmological Physics, University of Chicago, Chicago, IL USA*

I. DETAILS OF NUMERICAL ANALYSIS

A. Identifying Realistic Natural FN Textures

This section provides details on the method used to identify natural realistic FN textures for leptons.

We allow for FN charges up to 7 for charged leptons, 7 for RH neutrinos in type-I seesaw, and 9 for RH neutrinos in the Dirac case. These large charge values are necessary to produce the observed neutrino masses for $\epsilon \sim 0.1$.

Permutations of fields within a family do not represent physically distinct models. To remove these redundancies, we impose the following convention for the FN charges X_α, $\alpha \in \{L, e, N\}$: $|X_{\alpha_i}| \geq |X_{\alpha_j}|$ for $i < j$ when all X_α have the same sign, otherwise $X_{\alpha_i} \geq X_{\alpha_j}$. We also remove mirror charges, which are related by multiplying all charges by -1 and reordering them.

Each texture generates masses and mixings, which are compared to experimental values. Specifically, the observables we consider are the charged lepton masses, the PMNS matrix elements $|V_{11}|$, $|V_{13}|$, $|V_{23}|$, $|V_{21}|$, $|V_{31}|$, and $|V_{32}|$[1], the neutrino mass squared differences, $\Delta m^2_{21} = m_2^2 - m_1^2$ and $\Delta m^2_{32} = m_3^2 - m_2^2$, and the cosmological bound on the sum of neutrino masses. To account for scenarios where this bound may be relaxed [1–3], we also repeated our analyses using the laboratory bound [4]. The results show no significant differences. The measured values and uncertainties for these parameters are listed in Table I. For each observable $\mathcal{O}$, the fractional deviation from the experimental value is defined as

$$\delta_{\mathcal{O}} = \begin{cases} \exp\left|\ln\left(\frac{\mathcal{O}^{\rm FN}}{\mathcal{O}^{\rm exp}_{\rm min}}\right)\right| & \text{if } \mathcal{O}^{\rm FN} < \mathcal{O}^{\rm exp}_{\rm min}, \\ 1 & \text{if } \mathcal{O}^{\rm exp}_{\rm min} \leq \mathcal{O}^{\rm FN} \leq \mathcal{O}^{\rm exp}_{\rm max}, \\ \exp\left|\ln\left(\frac{\mathcal{O}^{\rm FN}}{\mathcal{O}^{\rm exp}_{\rm max}}\right)\right| & \text{if } \mathcal{O}^{\rm FN} > \mathcal{O}^{\rm exp}_{\rm max}. \end{cases} \tag{1}$$

* claudia.cornella@cern.ch
† dcurtin@physics.utoronto.ca
‡ krnjaicg@fnal.gov
§ m.mellors@mail.utoronto.ca

[1] Six PMNS elements are included because the uncertainties on these parameters are large enough that fitting only three independent elements, as would typically suffice for a unitary matrix, can still produce mixing matrices that deviate significantly from the measured values of the remaining elements.

Parameter	Exp. Value	Ref.
$m_e(1\text{ TeV})$	$0.489535765^{+0.000000013}_{-0.000000012}$ MeV	[5]
$m_\mu(1\text{ TeV})$	$103.3441945 \pm 0.0000059$ MeV	[5]
$m_\tau(1\text{ TeV})$	1756.81 ± 0.16 MeV	[5]
Δm^2_{21}	$(7.53 \pm 0.18) \times 10^{-5}$ eV^2	[6]
Δm^2_{32} (IO)	$(-2.536 \pm 0.034) \times 10^{-3}$ eV^2	[6]
Δm^2_{32} (NO)	$(2.453 \pm 0.033) \times 10^{-3}$ eV^2	[6]
$\sum m_\nu$ (cosmo)	≤ 0.12 eV (95% CL)	[6]
$\sum m_\nu$ (KATRIN)	≤ 1.35 eV (90% CL)	[4]
$\lvert V_{12}\rvert$	$[0.513, 0.579]$	[7]
$\lvert V_{13}\rvert$	$[0.143, 0.155]$	[7]
$\lvert V_{23}\rvert$	$[0.637, 0.776]$	[7]
$\lvert V_{21}\rvert$	$[0.234, 0.500]$	[7]
$\lvert V_{31}\rvert$	$[0.271, 0.525]$	[7]
$\lvert V_{32}\rvert$	$[0.477, 0.694]$	[7]

TABLE I: Measured parameters and their uncertainties. Charged lepton masses are evaluated at a scale of 1 TeV and PMNS elements are given in 3σ ranges. We conduct all analyses twice, either imposing the cosmology or laboratory bound on $\sum m_\nu$, and find no meaningful difference in our conclusions.

Here $\mathcal{O}^{\text{exp}}_{\text{min}}$ and $\mathcal{O}^{\text{exp}}_{\text{max}}$ are the experimental lower and upper bounds for the observable $\mathcal{O}$, respectively. We then scan over many possible coefficient choices c^α_{ij} as explained in the main text. Textures can then be ranked by $\mathcal{F}_x$ for different x.

B. Increasingly Focused Scan Sequence

For each mass mechanism, the numerical procedure described above is performed in several stages. This is necessary because the full parameter space is enormous: for example, in the Dirac case there are over 100 million distinct charge assignments $\{X_L, X_e, X_N\}$.

Scanning all textures in full (i.e. with a large number of trials) is numerically prohibitive, so we implement preliminary scans to discard unpromising textures early. A distinct numerical advantage of our approach is that, generically, relatively large values of $\mathcal{F}_x$ for different choices of x are highly correlated for natural realistic textures. This correlation allows us to perform an initial scan with few trials per texture, applying a cutoff at $\mathcal{F}_5$. Textures surpassing this initial threshold are then subjected to more intensive scrutiny for many more trials, focusing on $\mathcal{F}_x$ values for x very close to 1. This strategy not only conserves computational resources but also ensures that only the most promising textures are examined in depth. We validate this method a posteriori by confirming that it consistently identifies textures capable of providing exact fits to the data, as detailed in Appendix I D.

Charged lepton prescan – The first stage targets the charged lepton sector, where we start by examining 231,232 distinct charge assignments $\{X_L, X_{\bar{e}}\}$. This number can be reduced to 110,590 unique charge difference matrices n^ℓ_{ij}, as permutations and redundancies are removed. Matrices containing a zero difference produce an eigenvalue of the same order as the Higgs VEV, which is too large for the tau mass. Removing these yields ∼66k unique matrices, corresponding to ∼134k textures. We perform a charged lepton-only scan by

running 1000 coefficient trials per texture and computing $\mathcal{F}_x$ using only the charged lepton masses as observables. Textures are retained if they satisfy $\mathcal{F}_5 > 0$, meaning that at least a small fraction of trials match the charged lepton data. At this stage, $\sim$ 46k charge assignments $\{X_L, X_{\bar{e}}\}$ pass the $\mathcal{F}_5 > 0$ cut.

Secondary preselection – Next, we incorporate constraints from the neutrino sector and impose additional cuts, which depend on the specific mass mechanism.

- **Dirac** – For the Dirac case, since neutrino masses depend only on ϵ, the required charge differences n^ν must produce the appropriate level of suppression, $\epsilon^{n^\nu} \sim m_\nu$. For each charged lepton texture $\{X_L, X_{\bar{e}}\}$, we determine the allowed RH neutrino charges by identifying the minimal viable value of ϵ from the charged lepton prescan, denoted $\epsilon_{\min}$, that meets the criteria $\delta_{\max} < 5$. We then use $\epsilon_{\min}$ to compute the minimum charge difference n^ν that satisfies a conservative bound on the total neutrino mass (e.g. $m^\nu_{\lim} = 100 \sum m_\nu$). Any texture with charge differences n^ν below this minimum is discarded. This procedure drastically reduces the number of candidate textures $\{X_L, X_{\bar{e}}, X_N\}$ to $\sim$ 74k, corresponding to $\sim$ 35k unique charge difference matrices $\{n^\ell, n^\nu\}$.

- **Majorana** – In the Majorana scenario, there are no RH neutrino charges, so the neutrino charge differences n^W are determined directly from the LH charges X_L. After the charged lepton prescan, the top-performing textures are directly passed to the full scan without further cuts. The number of candidate charge difference matrices $\{n^\ell, n^W\}$ for the Majorana case is $\sim$94k.

- **Seesaw** – For type-I seesaw, the mass and mixing parameters depend on three charge difference matrices: n^ℓ (charged lepton Dirac), n^ν (neutrino Dirac), n^N (RH Majorana). The dependence of the neutrino masses on Λ prevents us from using cuts on $\epsilon_{\min}$ as was done in the Dirac case. Due to the enormous number of possibilities (over 64 million charge assignments for maximum charge 7, after the charged lepton prescan), a preliminary scan is performed. Specifically, we run a very coarse scan with 40 trials per texture, requiring $\mathcal{F}_5 > 10\%$. Only textures passing this criterion are subjected to the full scan with 1000 trials. This procedure retains $\sim$ 2.7 million textures for further analysis. Despite the looser cuts, we expect this approach to capture all relevant textures with $\mathcal{F}_5 > 50\%$.

Final scans – After the secondary preselection, we perform two more scans for all mass mechanisms. First, for each remaining texture, we do a fresh scan with 1000 coefficient choices and rank textures based on $\mathcal{F}_2$. Textures with the same $\mathcal{F}_2$ are ranked by $\mathcal{F}_5$. Finally, for the top 1000 textures from this prescan we do a final scan with 10^5 random coefficient choices. Textures are ranked by $\mathcal{F}_x$ with $x \approx 1.2 - 1.3$ depending on the FN scenario. The exact value of x is chosen to be as close to 1 as possible while optimizing the statistical significance of the ranking.

Our phenomenological analysis focuses solely on observables related to lepton flavor or lepton number violation. Specifically we include LFV processes at low and high energies and neutrinoless double β decay. The complete list of observables, alongside their current and projected experimental sensitivities, are summarized in Table II.

Observable	Current	Ref.	Future	Ref.
$\mathrm{BR}(\mu^+ \to e^+\gamma)$	4.2×10^{-13}	[8]	6×10^{-14}	[9]
$\mathrm{BR}(\mu^+ \to e^+e^-e^+)$	1.0×10^{-12}	[10]	10^{-16}	[11]
$\mathrm{BR}(\tau \to e\gamma)$	3.3×10^{-8}	[12]	2×10^{-9}	[13]
$\mathrm{BR}(\tau \to \mu\gamma)$	4.2×10^{-8}	[14]	10^{-9}	[13]
$\mathrm{BR}(\tau \to eee)$	2.7×10^{-8}	[15]	4×10^{-10}	[13]
$\mathrm{BR}(\tau \to \mu\mu\mu)$	2.1×10^{-8}	[15]	4×10^{-10}	[13]
$\mathrm{BR}(\tau^- \to \mu^+e^-\mu^-)$	2.7×10^{-8}	[15]	4×10^{-10}	[13]
$\mathrm{BR}(\tau^- \to e^+\mu^-\mu^-)$	1.7×10^{-8}	[15]	3×10^{-10}	[13]
$\mathrm{BR}(\tau^- \to e^+\mu^-e^-)$	1.8×10^{-8}	[15]	3×10^{-10}	[13]
$\mathrm{BR}(\tau^- \to \mu^+e^-e^-)$	1.5×10^{-8}	[15]	3×10^{-10}	[13]
$\mathrm{CR}(\mu^-\mathrm{Ti} \to e^-\mathrm{Ti})$	6.1×10^{-13}	[16]	-	-
$\mathrm{CR}(\mu^-\mathrm{Pb} \to e^-\mathrm{Pb})$	4.6×10^{-11}	[17]	-	-
$\mathrm{CR}(\mu^-\mathrm{Au} \to e^-\mathrm{Au})$	7.0×10^{-13}	[18]	-	-
$\mathrm{CR}(\mu^-\mathrm{Al} \to e^-\mathrm{Al})$	-	-	3×10^{-17}	[19]
m_{ee}	36 meV	[6]	3 meV	[20, 21]
$\mu\mu \to e\mu$	-	-	-	-
$\mu\mu \to \mu\tau$	-	-	-	-
$\mu\mu \to e\tau$	-	-	-	-

TABLE II: Current experimental limits and future sensitivities for the observables considered in our analysis. Current limits are given at 90% confidence level, except for the bound on m_{ee}, which is marginalized over different nuclear matrix element values with $\mathcal{O}(1)$ uncertainty.

C. Predicting Lepton Violation in FN

For the predictions, we employ the SMEFT framework. We construct effective operators following the power counting dictated by formal $U(1)_{\mathrm{FN}}$ invariance, as in

$$\mathcal{O}_4 = \frac{c_{ijkl}}{\Lambda^2} \left(\bar{\psi}_i \psi_j\right) \left(\bar{\psi}_k \psi_l\right) \epsilon^{n_{ijkl}}, \tag{2}$$

where c_{ijkl} are $\mathcal{O}(1)$ coefficients and we have defined

$$n_{ijkl} \equiv |X_{\psi_i} - X_{\psi_j} + X_{\psi_k} - X_{\psi_l}|. \tag{3}$$

We assume all Wilson coefficients to be $\mathcal{O}(1)$, and generate them randomly with the same priors used for the effective Yukawa coefficients. For simplicity, we consider only SMEFT operators that contribute at tree-level to our observables (we checked explicitly with `wilson` [23] that running effects do not affect our results significantly). We collect these operators in Table III.

To calculate low-energy LFV processes, such as muon and tau decays and muon-to-electron conversion in nuclei, we use `flavio` [24]. For high-energy collider observables, we follow Ref. [25]. As for $0\nu\beta\beta$, the effective Majorana mass m_{ee} is given by $m_{ee} = |\sum_i m_i V_{ei}^2|$.

To generate predictions for the top FN textures, we retain all trials of our final scan that meet the goodness of fit criterium $\delta_{\max} \leq 2$, storing the associated rotation matrices, ϵ, and, where applicable, $\Lambda_{(W)}$.[2] Trials are then ranked by $\delta_{\max}$, and for the top 500, we calculate

[2] We explicitly checked with the top few textures that performing exact fits, as detailed in Appendix I D, and using these exact fits as input for the phenomenological study did not significantly alter the results.

Q_{LL}	$\left(\bar{L}_p\gamma_\mu L_r\right)\left(\bar{L}_s\gamma^\mu L_t\right)$	$Q_{LQ}^{(1)}$	$\left(\bar{L}_p\gamma_\mu L_r\right)\left(\bar{Q}_s\gamma^\mu Q_t\right)$
Q_{ee}	$\left(\bar{e}_p\gamma_\mu e_r\right)\left(\bar{e}_s\gamma^\mu e_t\right)$	$Q_{LQ}^{(3)}$	$\left(\bar{L}_p\gamma_\mu\tau^I L_r\right)\left(\bar{Q}_s\gamma^\mu\tau^I Q_t\right)$
Q_{Le}	$\left(\bar{L}_p\gamma_\mu L_r\right)\left(\bar{e}_s\gamma^\mu e_t\right)$	Q_{He}	$\left(H^\dagger i\overleftrightarrow{D}_\mu H\right)\left(\bar{e}_p\gamma_\mu e_r\right)$
Q_{ed}	$\left(\bar{e}_p\gamma_\mu e_r\right)\left(\bar{d}_s\gamma^\mu d_t\right)$	$Q_{HL}^{(1)}$	$\left(H^\dagger i\overleftrightarrow{D}_\mu H\right)\left(\bar{L}_p\gamma_\mu L_r\right)$
Q_{eu}	$\left(\bar{e}_p\gamma_\mu e_r\right)\left(\bar{u}_s\gamma^\mu u_t\right)$	$Q_{HL}^{(3)}$	$\left(H^\dagger i\overleftrightarrow{D}^I_\mu H\right)\left(\bar{L}_p\tau^I\gamma_\mu L_r\right)$
Q_{Lu}	$\left(\bar{L}_p\gamma_\mu L_r\right)\left(\bar{u}_s\gamma^\mu u_t\right)$	Q_{eW}	$\left(\bar{L}_p\sigma^{\mu\nu}e_r\right)\tau^I H W^I_{\mu\nu}$
Q_{Ld}	$\left(\bar{L}_p\gamma_\mu L_r\right)\left(\bar{d}_s\gamma^\mu d_t\right)$	Q_{eB}	$\left(\bar{L}_p\sigma^{\mu\nu}e_r\right)H B_{\mu\nu}$
Q_{Qe}	$\left(\bar{Q}_p\gamma_\mu Q_r\right)\left(\bar{e}_s\gamma^\mu e_t\right)$		

TABLE III: Warsaw-basis SMEFT operators included in our analysis [22]. $SU(2)_L$ indices are indicated by $j,k=1,2$ where necessary. Flavor indices are given by p,r,s,t=1, 2, 3. For leptons we include all flavor combinations. For quarks we only include flavor-diagonal combinations of the three lightest quarks, as the corresponding Wilson coefficients are enough to capture the leading contribution to $\mu-e$ conversion in nuclei. All other operators are set to zero.

the suppression for the Wilson coefficients of the operators in Table III. Note that to remain as model-independent as possible we have excluded operators where the two quark fields have different chiralities, as these could be further suppressed if, for instance, the quarks carried FN charges. However, we explicitly verified that including these operators results in only a $\sim 5\%$ correction. We only included flavor diagonal quark operators for the same reason. After rotating to the mass basis, we derive the predictions for the observables in II. For each observable we find the average and standard deviation and compare it to data. This allows us to establish a lower bound on Λ for Dirac and Majorana scenarios, and to check whether the predictions for type-I seesaw models comply with current bounds. Note that our bounds on Λ are derived purely from processes involving SM states. Considering the phenomenology of the flavon itself may yield additional, but model-dependent, bounds [26].

D. Natural Fits

This section details the method for adjusting the coefficients c_{ij}^α ($\alpha=\ell,\nu,W,N$) to reproduce exactly the masses and mixing parameters in Table I. Our goal is to demonstrate that with minimal adjustments to the initial $\mathcal{O}(1)$ coefficients, the predictions for our top FN textures can be brought into full agreement with data.

For each mass generation mechanism, we focus on the top texture as ranked in the main text. We use a simplex minimization algorithm to refine the coefficients c_{ij}^α to fit the experimental values by minimizing the cost function in Eq. (1). We do this using as starting point 1000 coefficient sets from trials that yielded a promising $\delta_{\max}<2$.

To assess the extent of the adjustment needed, we introduce the parameter:

$$\eta=\log_{10}\frac{\max|c|}{\min|c|} \tag{4}$$

where c spans all the coefficients in the effective Yukawa matrices c^ℓ, c^ν, c^W, and c^N. His-

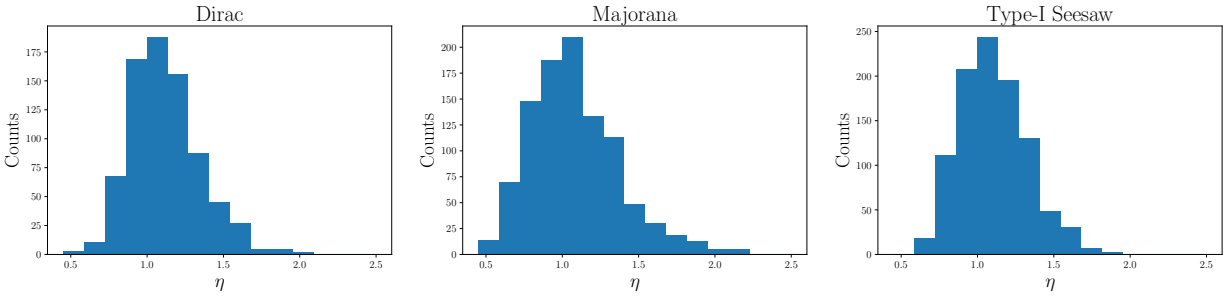

FIG. 1: Histograms of the η parameter distribution for 1000 trials that yield exact fits to the measured leptonic masses and mixings parameters. For each neutrino mass mechanism we show the result for the top-performing textures: for Dirac neutrinos (left), $X_L = \{6, 5, 5\}$, $X_e = \{-3, -2, 0\}$, $X_N = \{9, 8, 8\}$; for Majorana (middle), $X_L = \{2, 0, -1\}$, $X_e = \{7, 6, 4\}$; and for type-I seesaw (bottom), $X_L = \{6, 1, -1\}$, $X_e = \{7, 7, 6\}$, $X_N = \{3, 0, -4\}$.

tograms of η (Fig. 1) indicate that typically only a modest range variation is required, suggesting our selected textures reproduce experimental observations naturally, without extensive tuning or significant adjustments of coefficients. The examination of individual coefficient distributions further confirms that they adhere closely to our $\mathcal{O}(1)$ assumption. Overall, this check confirms our method of identifying natural and realistic textures without doing explicit fits to the experimental data.

II. MORE ON PHENOMENOLOGY AND SUPPLEMENTAL PLOTS

This appendix completes the discussion in the main text, supplementing the results with additional figures.

Low-energy CLFV and bounds on Λ – For both the Dirac and Majorana cases, the bounds on the FN scale Λ are set by current low-energy CLFV bounds. Fig. 2 illustrates that the strongest bounds are mostly set by $\mu \to e\gamma$ (and secondly by $\mu \to 3e$), with the strongest bound on Λ being remarkably consistent across different textures. The difference between the null and FN textures arises because FN observables sensitive to left-right couplings are suppressed with respect to the anarchic case.

Future muon colliders – Collider experiments provide a potential platform to test LFV processes predicted by FN models, especially at high energies where muon colliders [27] outshine e^+e^- colliders [28] due to their higher accessible energies and the resulting enhancement of cross-sections. Our analysis indicates that the Dirac and Majorana scenarios (with $\Lambda = \Lambda_{\rm exp}$), show the most promising but still very modest potential for detectable signals. Detailed results for these scenarios are illustrated in Fig. 3.

In Dirac FN models, certain textures exhibit an enhancement in the $\mu\tau$ final state. This enhancement is mainly due to the equality of X_{μ_L} and X_{τ_L} charges, which leads to significant contributions from unsuppressed LH four-fermion operators. As a result, $\mu\tau$ processes are more likely to be detected compared to $e\tau$ processes, which are generally suppressed by larger charge differences that diminish mixing. As shown in Fig. 3, we find $\mathcal{O}(1)$ and $\mathcal{O}(100)$ events for a c.o.m. energy of 10 and 100 TeV, respectively.

For Majorana neutrinos (with $\Lambda = \Lambda_{\rm exp}$), the predictions at colliders vary notably from

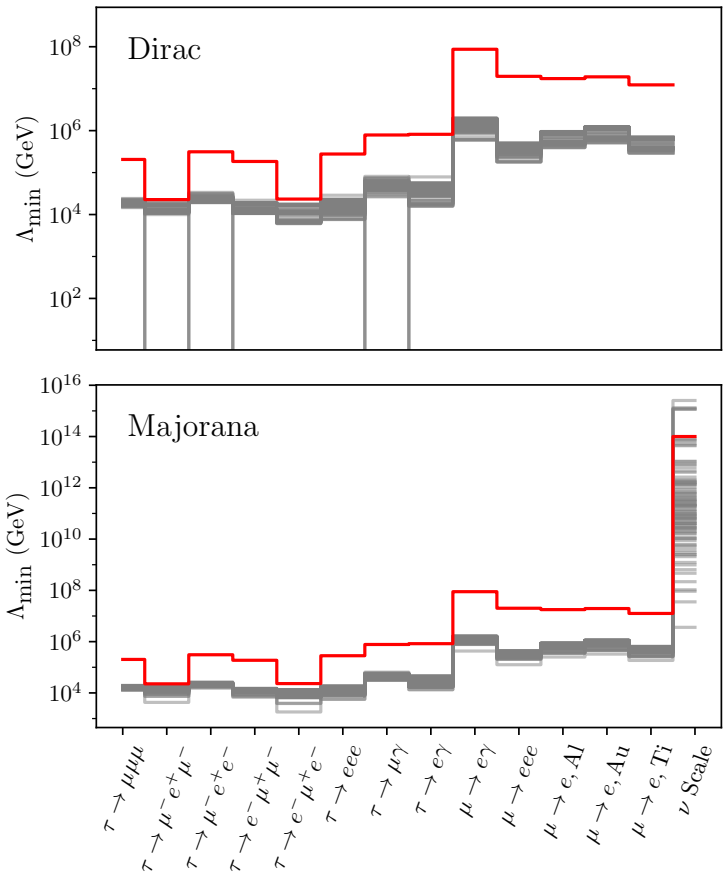

FIG. 2: Bounds on the FN scale Λ from current constraints on the processes shown on the horizontal axis, for the Dirac (top) and Majorana (bottom) FN scenarios. For the latter we also show the constraint from active neutrino masses if $\Lambda = \Lambda_W$.

those in the Dirac case. Here, the $e\mu$ and $\mu\tau$ final states are expected to have nearly similar magnitudes, reflecting the specific FN charge differences among LH fields. This similarity suggests that collider experiments could provide insights into the LH charge assignments in FN models. Still, collider prospects remain very limited, with only a few textures giving $\mathcal{O}(1)$ events at an extremely hypothetical 100 TeV machine.

Seesaw phenomenology – The phenomenology of the top 100 FN type-I seesaw models, detailed in Fig. 4, aligns broadly with that in the Dirac and Majorana cases (displayed in the main text), with less variability compared to the null texture. Unfortunately, none of the identified textures have a low enough scale to be probed by any currently planned CLFV experiment.

Active Neutrino Masses The predicted mass of the lightest neutrino and the sum of neutrino masses is shown in Fig. 5 for the top 100 textures of each mass mechanism. It is interesting to note that many of these natural realistic textures predict an ultralight active neutrino (see e.g. [29, 30]).

Dirac FN only predicts normal-ordered (NO) neutrinos. While DESI is projected to be able to measure the minimal NO scenario at 3σ [31], the resolution will not be sufficient to discriminate between Dirac textures. However, a positive determination of inverted-ordering (IO) would strongly disfavor the Dirac scenario.

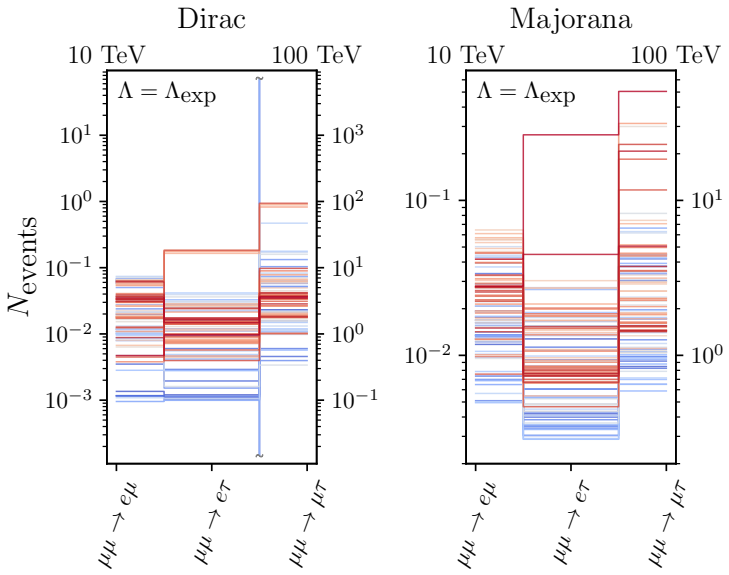

FIG. 3: Predicted muon collider event rates for CLFV processes in Dirac FN and Majorana FN scenarios with $\Lambda = \Lambda_{\rm exp} \neq \Lambda_W$ chosen to saturate current experimental bounds at $\Lambda \sim 10^6$ GeV. assuming an integrated luminosity of 10 ab^{-1}. In this figure, the ranking of each texture is indicated by color, with red textures ranked higher than blue textures. The corresponding results for the Majorana scenario with $\Lambda = \Lambda_W$ or type-I seesaw are not shown, as the predicted rates are many orders of magnitude smaller.

III. GENERALIZATIONS

A. Non-Trivially Charged Higgs

One can also consider the case where the Higgs is non-trivially charged under $U(1)_{\rm FN}$. For the Dirac case, the Lagrangian is modified to:

$$\mathcal{L} \supset -c^{\ell}_{ij} L_i H^\dagger \bar{e}_j \epsilon^{|X_{L_i} + X_{\bar{e}_j} - X_H|} - c^{\nu}_{ij} H L_i N_j \epsilon^{|X_{L_i} + X_{N_j} + X_H|} + \text{h.c.} \tag{5}$$

It is straightforward to identify textures with $X_H = 0$ that give equivalent Yukawas. Requiring all fields of the same type to be shifted by the same amount (e.g. $X_{L_i} \to X_{L_i} + c$), there are three possible solutions, depending on whether X_L, X_e or X_N is held fixed. Using X to denote the original $X_H = 0$ texture and X' to indicate the new $X_H \neq 0$ texture, the three solutions are as follows:

$$\begin{aligned}
&X'_{L_i} = X_{L_i}, \quad X'_{e_j} = X_{\bar{e}_j} - X_H, \quad X'_{N_j} = X_{N_j} + X_H, \\
&X'_{L_i} = X_{L_i} + X_H, \quad X'_{e_j} = X_{\bar{e}_j} - 2X_H, \quad X'_{N_j} = X_{N_j}, \\
&X'_{L_i} = X_{L_i} - X_H, \quad X'_{e_j} = X_{\bar{e}_j}, \quad X'_{N_j} = X_{N_j} + 2X_H.
\end{aligned} \tag{6}$$

For a given $X_H = 0$ texture from our analysis, we can then easily find the corresponding $X_H \neq 0$ textures. In the Majorana and type-I seesaw cases, the requirement that the Weinberg operator or the Majorana RH neutrino mass term remains invariant selects the second solution in Eq. (6).

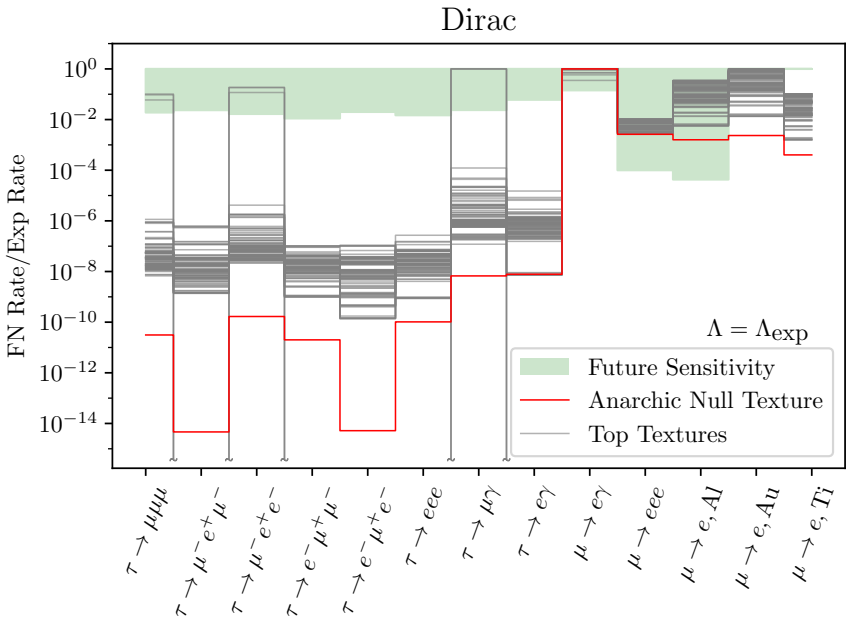

FIG. 4: Average predicted CLFV decay rates for the 100 most realistic natural type-I seesaw FN textures (gray lines), relative to each observable's current constraint. The FN scale Λ is fixed by neutrino masses. . Green shading indicates the reach of proposed future low-energy CLFV experiments, and the flavor-anarchic null texture is shown as a red line for comparison.

The purely leptonic observables for the $X_H = 0$ texture and the equivalent $X_H \neq 0$ textures remain the same. This can be seen by observing that most fermion bilinears are unaffected:

$$\begin{aligned}(\bar{\psi}_i \psi_j)\epsilon^{|X'_{\psi_j} - X'_{\psi_i}|} &= (\bar{\psi}_i \psi_j)\epsilon^{|(X_{\psi_j}+c)-(X_{\psi_i}+c)|}, \\ &= (\bar{\psi}_i \psi_j)\epsilon^{|X_{\psi_j} - X_{\psi_i}|}.\end{aligned} \tag{7}$$

Here, Dirac structures are omitted for clarity. As long as ψ_i, ψ_j are of the same type (e.g. $\bar{L}L$ or $\bar{e}e$), the shift cancels in the exponent, and the bilinear remains invariant. Thus, all four-fermion operators in Table III are unchanged. Similarly, the operators Q_{eW} and Q_{eB} share the same form as the Yukawa couplings, and are therefore invariant by definition. The remaining operators contain bilinears of the form $H^\dagger H$, which are $U(1)_{\rm FN}$-neutral by construction. As all SMEFT operators we consider remain the same, the predictions for CLFV are unchanged.

B. Other Sources of Lepton Number Violation

In the type-I seesaw case, we have assumed no additional sources of lepton number violation beyond the Majorana mass of the RH neutrino. If this assumption is relaxed, the Lagrangian is modified by an additional contribution to the Weinberg operator:

$$\mathcal{L} \supset \mathcal{L}_{\rm SS} - \frac{c_{ij}^W \epsilon^{n_{ij}^W}}{\Lambda_{\not L}} (L_i H)(L_j H)\,, \tag{8}$$

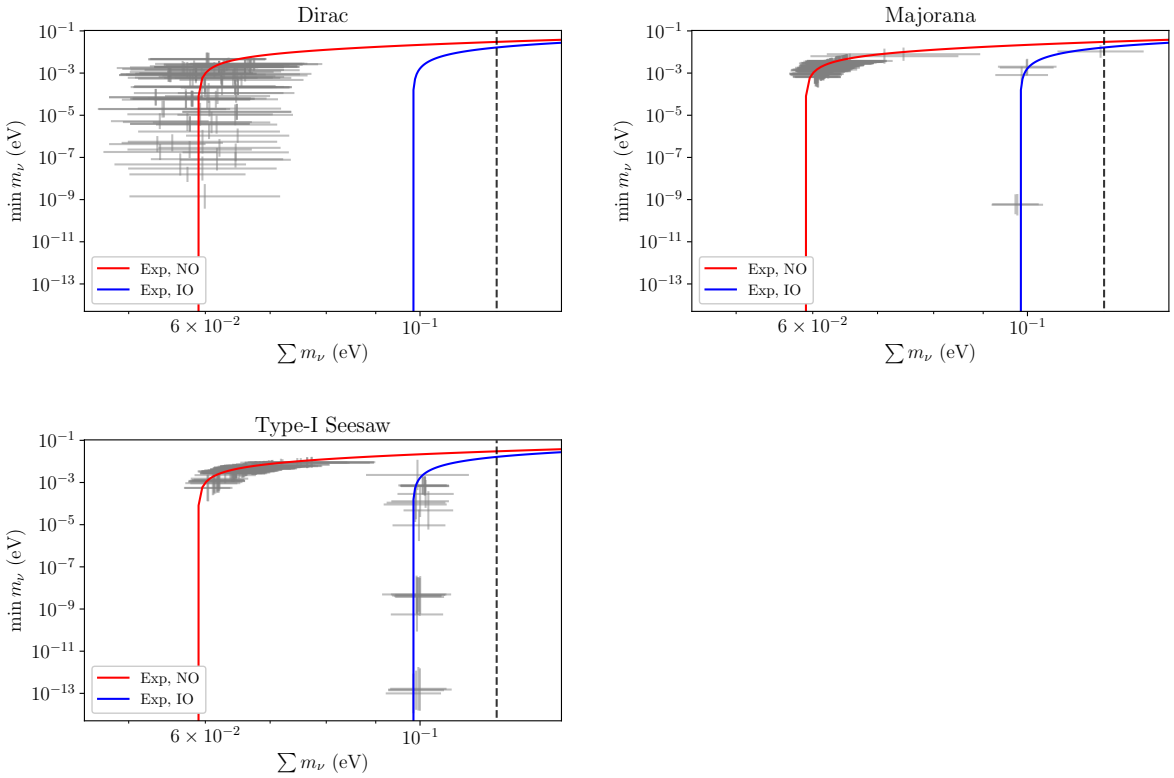

FIG. 5: Predictions for the lightest neutrino mass versus the sum of neutrino masses for the 100 most realistic textures in the Dirac (top), Majorana (middle) and type-I seesaw (bottom) FN scenarios. The red (blue) line represents the mass of the lightest neutrino as implied by the values of Δm^2_{21} and Δm^2_{32} for a $\sum m_\nu$ in the NO (IO) case. The dashed line shows the current cosmological constraint on the sum of neutrino masses. Error bars show the 1σ spread of predictions over 500 trials with $\delta_{\max} < 2$. The large error bars on the Dirac scenario are due to the high powers of ϵ required to reproduce neutrino masses, making this scenario more sensitive to small variations in ϵ.

where $\Lambda_{\not L}$ indicates the scale of the additional lepton number violation.

The resulting neutrino masses can be derived similarly to those in the type-I seesaw discussed in the main text. We define the Weinberg mass as $m^2_{W,ij} = v^2 c^W_{ij} \epsilon^{n^W_{ij}}$ and note that the Weinberg operator does not contribute to the mixing between sterile and active eigenstates until $\mathcal{O}\left((v\Lambda^{-1})^3\right)$ [32]. The resulting neutrino masses are:

$$m_\nu \approx \frac{m^2_W}{\Lambda_{\not L}} - m_D M_N^{-1} m_D^T \,, \tag{9}$$

where $m_D = vY^\nu/\sqrt{2}$ and $M_N = Mc^M \epsilon^{n^M}$.

We performed our analysis in the case where $\Lambda_{\not L} = \Lambda = M$, and found slightly different top textures. However, the overall conclusions remain unchanged: the scale of flavor violation for these models exceeds projected experimental sensitivities. The CLFV phenomenology for the top 100 textures is shown in Fig. 6.

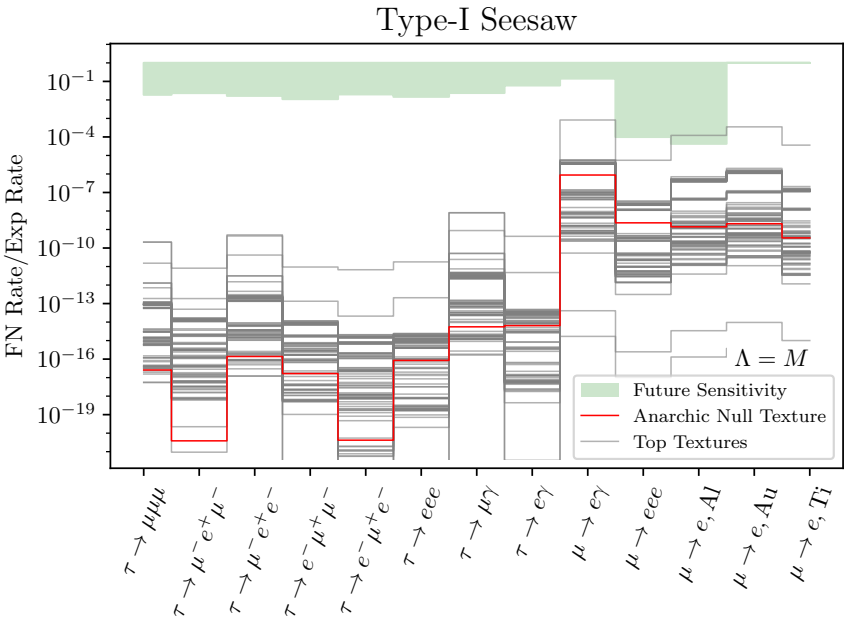

FIG. 6: Phenomenology for the top 100 type-I seesaw textures if the FN sector is lepton number violating (with $\Lambda_{\not L} = \Lambda = M$), as in Fig. 4. The FN scale Λ is fixed by neutrino masses. The axes are fixed to be the same as in Fig. 4 for ease of comparison.

C. Type II Seesaw and other Majorana UV Completions

The Majorana case can arise from a variety of UV completions. For illustration, we consider the example of a FN-augmented type-II seesaw mechanism. The type-II seesaw [33–37] has the form [38]

$$\mathcal{L}_{SS2} \supset -\frac{y}{2}\Delta LL - \mu_\Delta \Delta H^\dagger H^\dagger - M_\Delta^2 \mathrm{Tr}[\Delta^\dagger \Delta], \tag{10}$$

where Δ is an electroweak scalar triplet with hypercharge 1, and generation indices are omitted. The quantities M_Δ and μ_Δ are dimensionful, and y is dimensionless. When M_Δ is large, integrating out Δ yields a Weinberg operator with the prefactor:

$$\frac{c_2^W}{\Lambda_W} = \frac{2y\mu_\Delta}{M_\Delta^2}. \tag{11}$$

Assuming that Δ is charged under $U(1)_{FN}$, the Lagrangian becomes

$$\mathcal{L}_{SS2} \supset -\frac{y_{ij}}{2}\epsilon^{|X_{Li}+X_{Lj}+X_\Delta|} L_i L_j \Delta - c_\mu \Lambda \epsilon^{|X_\Delta|} \Delta H^\dagger H^\dagger + \text{h.c.} - (c_M \Lambda)^2 \mathrm{Tr}[\Delta^\dagger \Delta]. \tag{12}$$

where we have taken the mass scales μ_Δ and M_Δ to be set by the flavon scale Λ, and $y,\ c_\mu,\ c_M$ are $\mathcal{O}(1)$ prefactors. This implies the Weinberg coefficient

$$\begin{aligned}\frac{c_2^W}{\Lambda_W} &\approx \frac{2\left(y_{ij}\epsilon^{|X_{Li}+X_{Lj}+X_\Delta|}\right)\left(c_\mu\Lambda\epsilon^{|X_\Delta|}\right)}{(c_M\Lambda)^2} \\ &\approx \frac{\tilde{c}_{ij}\epsilon^{n^W+2X_\Delta}}{\Lambda},\end{aligned} \tag{13}$$

where $\tilde{c} \sim \mathcal{O}(1)$. In the second equality we have assumed all relevant charges to be positive, so that the absolute value can be dropped. As a result, the apparent scale of the Weinberg operator differs from the true FN scale by $\Lambda_W = \epsilon^{-2X_\Delta}\Lambda$. Consequently, a given effective Weinberg scale can correspond to a much lower physical scale. However, if charges are such that the absolute values in the exponents cannot be dropped, different generations may have distinct FN suppression. This scenario cannot be mapped onto our generic Majorana textures and lies beyond the scope of this work.

For the type-I seesaw, the same analysis yields:

$$\frac{c_2^W}{\Lambda_W} = \frac{1}{\Lambda}\left[c_{ij}^\nu\epsilon^{|X_{L_i}+X_{N_j}|}\left(c_{jm}^M\epsilon^{|X_{N_j}+X_{N_m}|}\right)^{-1}c_{mn}^\nu\epsilon^{|X_{L_n}+X_{N_{Rm}}|}\right] .$$

As in type-II seesaw, certain textures can be directly matched to a Majorana texture with a common scale. However, for some textures the effective scales are hierarchical and cannot be mapped onto the Majorana case as implemented in our method. Additionally, in some cases, a midscale UV completion of the Weinberg operator may generate additional contributions less suppressed than the FN-generated ones. In such cases, the phenomenological predictions would be somewhat different, depending on which operators are generated. These scenarios would require an ad-hoc study.

IV. AUXILIARY MATERIAL

In the auxiliary material we include several additional documents for reference. The files

- `dirac_tex_pheno_cosmo.csv`
- `seesaw_tex_pheno_cosmo.csv`
- `majorana_tex_pheno_cosmo.csv`

provide phenomenological predictions for each neutrino mass generation model. Each file contains the charge assignments for the top 100 textures, along with the best values of ϵ and Λ, when relevant, averaged over trials with $\delta_{\max} < 2$. NO indicates the fraction of trials that yield normal-ordered neutrinos. $\Lambda_{\exp}$ is the scale implied by the most constraining observable. By default charge assignments are sorted by $\mathcal{F}_x$, where x is the lowest value for which at least 25 coefficient choices satisfy the criterion $\delta_{\max} < x$. $\mathcal{F}_2$ and $\mathcal{F}_5$ are also provided. All dimensionful quantities are given in GeV. Collider observables are the estimated number of events at an extremely hypothetical 100 TeV muon collider with 10^{-1} ab integrated luminosity. Branching fractions and conversion rates are calculated assuming that the scale is set by $\Lambda_{\exp}$ for the most constraining observable (usually $\mu \to e\gamma$) for the Dirac and Majorana cases, and by the scale implied by neutrino masses for the type-I seesaw case. All results are given assuming the cosmological bound on neutrino masses.

Correlation plots for the top 100 textures of each neutrino mass model are included in the files:

- `dirac_correlations_cosmo.pdf`
- `majorana_correlations_cosmo.pdf`

These plots show the values of observables for the top 500 trials (smallest $\delta_{\max}$) for each texture, smoothed using a Gaussian kernel estimation to determine approximate 1σ (solid line) and 2σ (dashed line) predictions. Shaded regions indicate parameter space that may be probed in future experiments and solid horizontal/vertical lines indicate current constraints. The constraint on the muon conversion rate in aluminum is estimated based on current constraints in gold. Collider observables are as above. The scale is set as above.

Correlation plots for the seesaw model are not included, as nearly all textures fall outside experimental observation.

---

[1] I. M. Oldengott, G. Barenboim, S. Kahlen, J. Salvado, and D. J. Schwarz, "How to relax the cosmological neutrino mass bound," *JCAP* **04** no. 04, (Apr., 2019) 049, arXiv:1901.04352 [astro-ph.CO].

[2] Z. Chacko, A. Dev, P. Du, V. Poulin, and Y. Tsai, "Cosmological Limits on the Neutrino Mass and Lifetime," *JHEP* **04** (Apr., 2020) 020, arXiv:1909.05275 [hep-ph].

[3] M. Escudero, T. Schwetz, and J. Terol-Calvo, "A seesaw model for large neutrino masses in concordance with cosmology," *JHEP* **02** no. 2, (Feb., 2023) 142, arXiv:2211.01729 [hep-ph].

[4] **Katrin** Collaboration, M. Aker *et al.*, "Direct neutrino-mass measurement based on 259 days of KATRIN data," arXiv:2406.13516 [nucl-ex].

[5] Z.-z. Xing, H. Zhang, and S. Zhou, "Impacts of the Higgs mass on vacuum stability, running fermion masses and two-body Higgs decays," *Phys. Rev. D* **86** no. 1, (2012) 013013, arXiv:1112.3112 [hep-ph].

[6] **Particle Data Group** Collaboration, R. L. Workman *et al.*, "Review of Particle Physics," *PTEP* **2022** (Aug., 2022) 083C01.

[7] I. Esteban, M. Gonzalez-Garcia, M. Maltoni, T. Schwetz, and A. Zhou, "The fate of hints: Updated global analysis of three-flavor neutrino oscillations," *JHEP* **09** no. 9, (Sept., 2020) 178, arXiv:2007.14792 [hep-ph].

[8] **MEG** Collaboration, A. M. Baldini *et al.*, "Search for the lepton flavour violating decay $M^+ \to e^+\gamma$ with the full dataset of the MEG experiment," *Eur. Phys. J. C* **76** no. 8, (Aug., 2016) 434, arXiv:1605.05081 [hep-ex].

[9] A. M. Baldini *et al.*, "MEG Upgrade Proposal," arXiv:1301.7225 [physics.ins-det].

[10] **SINDRUM** Collaboration, U. Bellgardt, G. Otter, *et al.*, "Search for the decay $\mu^+ \to e^+e^+e^-$," *Nucl. Phys. B* **299** no. 1, (1988) 1–6.

[11] A. Blondel *et al.*, "Research Proposal for an Experiment to Search for the Decay $\mu \to eee$," arXiv:1301.6113 [physics.ins-det].

[12] **BaBar** Collaboration, B. Aubert *et al.*, "Searches for Lepton Flavor Violation in the Decays $T^+ \to e^+\gamma$ and $\tau^+ \to M^+\gamma$," *Phys. Rev. Lett.* **104** (2010) 021802, arXiv:0908.2381 [hep-ex].

[13] **Belle-II** Collaboration, E. Kou, P. Urquijo, *et al.*, "The Belle II Physics Book," *PTEP* **2019** no. 12, (Dec., 2019) 123C01, arXiv:1808.10567 [hep-ex].

[14] **Belle** Collaboration, K. Uno, K. Hayasaka, *et al.*, "Search for lepton-flavor-violating tau-lepton decays to $\ell\gamma$ at Belle," *JHEP* **10** no. 10, (2021) 19, arXiv:2103.12994 [hep-ex].

[15] K. Hayasaka *et al.*, "Search for Lepton Flavor Violating Tau Decays into Three Leptons with 719 Million Produced Tau+Tau- Pairs," *Phys. Lett. B* **687** (2010) 139–143, arXiv:1001.3221 [hep-ex].

[16] P. Wintz, "Results of the SINDRUM-II experiment," *Conf. Proc. C* **980420** (1998) 534–546.

[17] **SINDRUM II** Collaboration, W. Honecker *et al.*, "Improved limit on the branching ratio of μ-e conversion on lead," *Phys. Rev. Lett.* **76** (1996) 200–203.

[18] **SINDRUM II** Collaboration, W. Bertl, R. Engfer, *et al.*, "A search for μ-e conversion in muonic gold," *Eur. Phys. J. C* **47** no. 2, (2006) 337–346.

[19] **Mu2e** Collaboration, L. Bartoszek, E. Barnes, *et al.*, "Mu2e Technical Design Report," arXiv:1501.05241 [physics.ins-det].

[20] **nEXO** Collaboration, n. Collaboration, G. Adhikari, *et al.*, "NEXO: Neutrinoless double beta decay search beyond 10^{28} year half-life sensitivity," *J. Phys. G* **49** no. 1, (Dec., 2021) 015104, arXiv:2106.16243 [nucl-ex].

[21] **CUPID** Collaboration, A. Armatol, C. Augier, *et al.*, "Toward CUPID-1T," arXiv:2203.08386 [nucl-ex].

[22] B. Grzadkowski, M. Iskrzynski, M. Misiak, and J. Rosiek, "Dimension-Six Terms in the Standard Model Lagrangian," *JHEP* **10** no. 10, (2010) 085, arXiv:1008.4884 [hep-ph].

[23] J. Aebischer, J. Kumar, and D. M. Straub, "Wilson: A Python package for the running and matching of Wilson coefficients above and below the electroweak scale," *Eur. Phys. J. C* **78** no. 12, (Dec., 2018) 1026, arXiv:1804.05033 [hep-ph].

[24] D. M. Straub, "Flavio: A Python package for flavour and precision phenomenology in the Standard Model and beyond," arXiv:1810.08132 [hep-ph].

[25] M. Paraskevas, "Dirac and Majorana Feynman Rules with four-fermions," arXiv:1802.02657 [hep-ph].

[26] M. Heikinheimo, K. Huitu, V. Keus, and N. Koivunen, "Cosmological constraints on light flavons," *JHEP* **06** (2019) 065, arXiv:1812.10963 [hep-ph].

[27] C. Accettura *et al.*, "Towards a muon collider," *Eur. Phys. J. C* **83** no. 9, (2023) 864, arXiv:2303.08533 [physics.acc-ph]. [Erratum: Eur.Phys.J.C 84, 36 (2024)].

[28] V. Shiltsev and F. Zimmermann, "Modern and Future Colliders," *Rev. Mod. Phys.* **93** no. 1, (Mar., 2021) 015006, arXiv:2003.09084 [physics.acc-ph].

[29] Z. Chacko, N. Craig, P. J. Fox, and R. Harnik, "Cosmology in Mirror Twin Higgs and Neutrino Masses," *JHEP* **07** (2017) 023, arXiv:1611.07975 [hep-ph].

[30] G. Alonso-Álvarez, D. Curtin, A. Rasovic, and Z. Yuan, "Baryogenesis through Asymmetric Reheating in the Mirror Twin Higgs," *JHEP* **05** (May, 2024) 069, arXiv:2311.06341 [hep-ph].

[31] **DESI** Collaboration, A. Aghamousa *et al.*, "The DESI Experiment Part I: Science,Targeting, and Survey Design," arXiv:1611.00036 [astro-ph.IM].

[32] A. Dedes, S. Rimmer, and J. Rosiek, "Neutrino masses in the Lepton Number Violating MSSM," *JHEP* **08** (2006) 005, arXiv:hep-ph/0603225.

[33] M. Magg and C. Wetterich, "Neutrino Mass Problem and Gauge Hierarchy," *Phys. Lett. B* **94** (1980) 61–64.

[34] J. Schechter and J. W. F. Valle, "Neutrino Masses in SU(2) x U(1) Theories," *Phys. Rev. D* **22** (1980) 2227.

[35] G. Lazarides, Q. Shafi, and C. Wetterich, "Proton Lifetime and Fermion Masses in an

SO(10) Model," *Nucl. Phys. B* **181** (1981) 287–300.

[36] R. N. Mohapatra and G. Senjanovic, "Neutrino Masses and Mixings in Gauge Models with Spontaneous Parity Violation," *Phys. Rev. D* **23** (1981) 165.

[37] C. Wetterich, "Neutrino Masses and the Scale of B-L Violation," *Nucl. Phys. B* **187** (1981) 343–375.

[38] E. Ma and U. Sarkar, "Neutrino Masses and Leptogenesis with Heavy Higgs Triplets," *Phys. Rev. Lett.* **80** no. 26, (1998) 5716–5719, arXiv:hep-ph/9802445.